Title

Asymmetric susceptibility tensor imaging

Journal

Magnetic Resonance in Medicine, 86(4)

ISSN

0740-3194

Authors

Cao, Steven
Wei, Hongjiang
Chen, Jingjia
et al.

Publication Date

2021-10-01

DOI

10.1002/mrm.28823

Peer reviewed

HHS Public Access

Author manuscript

Magn Reson Med. Author manuscript; available in PMC 2021 December 17.

Published in final edited form as:

Magn Reson Med. 2021 October ; 86(4): 2266–2275. doi:10.1002/mrm.28823.

Asymmetric susceptibility tensor imaging

Steven Cao[1], **Hongjiang Wei**[1,2], **Jingjia Chen**[1], **Chunlei Liu**[1,3]

[1]Department of Electrical Engineering and Computer Sciences, University of California, Berkeley, California, USA

[2]Institute for Medical Imaging Technology, School of Biomedical Engineering, Shanghai Jiao Tong University, Shanghai, China

[3]Helen Wills Neuroscience Institute, University of California, Berkeley, California, USA

Abstract

Purpose: To investigate the symmetry constraint in susceptibility tensor imaging.

Theory: The linear relationship between the MRI frequency shift and the magnetic susceptibility tensor is derived without constraining the tensor to be symmetric. In the asymmetric case, the system matrix is shown to be maximally rank 6. Nonetheless, relaxing the symmetry constraint may still improve tensor estimation because noise and image artifacts do not necessarily follow the constraint.

Methods: Gradient echo phase data are obtained from postmortem mouse brain and kidney samples. Both symmetric and asymmetric tensor reconstructions are applied to the data. The reconstructions are then used for susceptibility tensor imaging fiber tracking. Simulations with ground truth and at various noise levels are also performed. The reconstruction methods are compared qualitatively and quantitatively.

Results: Compared to regularized and unregularized symmetric reconstructions, the asymmetric reconstruction shows reduced noise and streaking artifacts, better contrast, and more complete fiber tracking. In simulation, the asymmetric reconstruction achieves better mean squared error and better angular difference in the presence of noise. Decomposing the asymmetric tensor into its symmetric and antisymmetric components confirms that the underlying susceptibility tensor is symmetric and that the main sources of asymmetry are noise and streaking artifacts.

Conclusion: Whereas the susceptibility tensor is symmetric, asymmetric reconstruction is more effective in suppressing noise and artifacts, resulting in more accurate estimation of the susceptibility tensor.

Keywords

asymmetric susceptibility tensor; image reconstruction; streaking artifacts; susceptibility tensor imaging

Correspondence: Chunlei Liu, Department of Electrical Engineering and Computer Sciences, University of California, 505 Cory Hall, Berkeley, CA 94720, USA. chunlei.liu@berkeley.edu.

SUPPORTING INFORMATION

Additional supporting information may be found online in the Supporting Information section.

1 | INTRODUCTION

Susceptibility tensor imaging (STI) is a recently developed MRI technique that measures anisotropic magnetic susceptibility with a tensor model.[1] Scalar magnetic susceptibility measured in a single B_0-field direction, achieved by quantitative susceptibility mapping (QSM), has been shown to be sensitive to iron content, myelin, and collagen fibril organization, making it useful for the study of a multitude of diseases, including Parkinson's, Alzheimer's, multiple sclerosis, fibrosis, and osteoarthritis.[2–10] However, magnetic susceptibility is anisotropic in some tissues and therefore must be described by a tensor.[1,5,11–15] Susceptibility tensor tractography has been shown to convey information about white matter tracts, kidney tubules, myofibers, and fibers not encapsulated by diffusion-based tractography.[16–19]

Despite this promise, reconstruction of the susceptibility tensor from multi-orientation phase maps faces many challenges due to low SNR, especially in the off-diagonal terms, and vulnerability to streaking artifacts. Injection of a gadolinium-based contrast agent improves contrast,[20] but this is at the cost of imaging artifacts in areas where the contrast agent accumulates and alteration of native susceptibility values. These problems distort underlying structures and make fiber tracking difficult.

Multiple regularization schemes have been proposed to produce better tensor images. In one such study, Liu et al propose a regularization term that penalizes tensor anisotropy at higher frequencies.[18] This approach produces more smoothly varying tensor images, allowing for better and more complete fiber tracking. However, this increased SNR comes at the cost of significant blurring and relies on the assumption that the tensor's anisotropic terms spatially are slowly varying. In another study, Li et al assume that only white matter is anisotropic and regularizes accordingly to enforce this assumption, resulting in more uniform tensor maps.[21] The drawback of this approach is that it makes a strong assumption about susceptibility and is not applicable outside the brain. Another approach is to regularize the eigenvector orientation of the susceptibility tensor to be similar to that of the diffusion tensor.[22–24] However, this approach relies on the assumption that the 2 tensors have similar directions, which is not true for all tissues. Finally, Dibb et al propose a joint estimation technique where the susceptibility and relaxation tensors are jointly solved for with the assumption that they share an eigenvector.[19] This approach produces improved tractography but uses additional relaxation data that is even noisier. Additionally, it uses the regularization proposed in Ref. 18; thus, it shares the same drawback of reduced contrast. Overall, these approaches are not sufficient to produce fully satisfactory tensor maps and rely on strong assumptions, making further work necessary.

In this study, we exploit the symmetry of the susceptibility tensor to present a new STI reconstruction algorithm that produces higher SNR and improved anatomical contrast without regularization. The susceptibility tensor of white matter has been assumed to be symmetric due to the cylinder-like geometry of myelinated axons; thus, current approaches impose a symmetry constraint during inversion.[1] We propose an inversion algorithm without this constraint, termed *asymmetric STI* (aSTI), and instead enforce symmetry post-inversion

by decomposing the result into symmetric and antisymmetric parts. We justify this approach empirically by comparing reconstructions of mouse brain and kidney data.

2 | THEORY

2.1 | Phase-susceptibility relationship without the symmetry constraint

The degree to which materials magnetize in response to a magnetic field is called *magnetic susceptibility and denoted* $\boldsymbol{\chi}$. Because susceptibility is inhomogeneous across a heterogeneous sample, magnetization in response to the B_0 field is also inhomogeneous, producing phase variations measurable using MRI. In this section, we derive the phase-susceptibility relationship (for details, see Refs. 1,5).

Given some applied field $\vec{B}_0 = B_0\hat{H}$ with strength B_0 and unit direction $\hat{H}$, a point source with susceptibility tensor $\boldsymbol{\chi}$ has magnetization μ given by

$$\mu = \chi\vec{B}_0, \tag{1}$$

where $\boldsymbol{\chi}$ is a 3 × 3 tensor given by

$$\chi = \begin{bmatrix} \chi_{11} & \chi_{12} & \chi_{13} \\ \chi_{21} & \chi_{22} & \chi_{23} \\ \chi_{31} & \chi_{32} & \chi_{33} \end{bmatrix}. \tag{2}$$

Magnetized material acts as a dipole. Therefore, the field perturbation resulting from a collection of point sources can be found by convolving the dipole magnetic field kernel with the magnetization distribution, which in the Fourier domain becomes multiplication. Then, using the vector $\vec{k} = [k_1 k_2 k_3]^T$ to represent the coordinate in the Fourier domain, the resulting field perturbation in the Fourier domain at $\vec{k}$ is given by

$$\Delta\vec{B}_k(\vec{k}) = \left(\frac{1}{3}\mathbf{I} - \frac{\vec{k}\vec{k}^T}{\vec{k}^T\vec{k}}\right)\boldsymbol{\chi}_{\boldsymbol{k}}(\vec{k})B_0\hat{H}, \tag{3}$$

where $\boldsymbol{\chi}_{\boldsymbol{k}}$ is the elementwise Fourier transform of $\boldsymbol{\chi}$ and $\mathbf{I}$ is the identity matrix. Only the field perturbation in the $\hat{H}$ direction produces a measurable frequency shift; therefore, we project the field perturbation to get

$$\Delta B_k(\vec{k}) = \hat{H}^T\left(\frac{1}{3}\mathbf{I} - \frac{\vec{k}\vec{k}^T}{\vec{k}^T\vec{k}}\right)\boldsymbol{\chi}_{\boldsymbol{k}}(\vec{k})B_0\hat{H}. \tag{4}$$

This field perturbation is proportional to the frequency shift, which is proportional to the phase shift, which we can measure. We can then invert this relationship and apply the inverse Fourier transform to recover the susceptibility at each point in the imaged object.

Equation (4) is linear in the 9 terms of $\chi_{\boldsymbol{k}}(\hat{k})$ Therefore, we can apply the magnetic field in multiple directions $\hat{H}^{(1)},\ldots,\hat{H}^{(n)}$ and stack the equation n times to form a matrix-vector equation $\overrightarrow{b} = \mathbf{A}\overrightarrow{x}$ given by

$$\begin{bmatrix} \Delta B_k^{(1)}(\overrightarrow{k}) \\ \vdots \\ \Delta B_k^{(n)}(\overrightarrow{k}) \end{bmatrix} = \begin{bmatrix} \frac{H_1^{(1)}H_1^{(1)}}{3} - \frac{k_1 H_1^{(1)}}{\overrightarrow{k}^T\overrightarrow{k}}\overrightarrow{k}^T\widehat{H}^{(1)} & \cdots & \frac{H_3^{(1)}H_3^{(1)}}{3} - \frac{k_3 H_3^{(1)}}{\overrightarrow{k}^T\overrightarrow{k}}\overrightarrow{k}^T\widehat{H}^{(1)} \\ \vdots & \ddots & \vdots \\ \frac{H_1^{(n)}H_1^{(n)}}{3} - \frac{k_1 H_1^{(n)}}{\overrightarrow{k}^T\overrightarrow{k}}\overrightarrow{k}^T\widehat{H}^{(n)} & \cdots & \frac{H_3^{(n)}H_3^{(n)}}{3} - \frac{k_3 H_3^{(n)}}{\overrightarrow{k}^T\overrightarrow{k}}\overrightarrow{k}^T\widehat{H}^{(n)} \end{bmatrix} \begin{bmatrix} \chi_k(\overrightarrow{k})_{11} \\ \vdots \\ \chi_k(\overrightarrow{k})_{33} \end{bmatrix}, \tag{5}$$

where the matrix $\mathbf{A}$ has dimension $n \times 9$. If the susceptibility tensor is symmetric ($\boldsymbol{\chi}^T = \boldsymbol{\chi}$), then instead of solving for 9 elements of the susceptibility tensor, we only need to solve for 6,

$$\overrightarrow{x'} = [\chi_{11}\chi_{12} + \chi_{21}\chi_{13} + \chi_{31}\chi_{22}\chi_{23} + \chi_{32}\chi_{33}]^T \tag{6}$$

by combining the corresponding columns of the matrix in Equation (5), turning it into the matrix $\mathbf{A}'$ with dimension $n \times 6$. The $n \geq 6$ directions can be chosen such that the matrix is well conditioned, so we take the least squares solution $\overrightarrow{x'} = \left(\mathbf{A}'^T\mathbf{A}'\right)^{-1}\mathbf{A}'^T\overrightarrow{b}$.

2.2 | The phase-susceptibility relationship is rank-deficient

If the susceptibility tensor is not symmetric, we can solve Equation (5) without combining the off-diagonal terms. However, in this case the inversion is ill posed because the phase-susceptibility system matrix $\mathbf{A}$ is maximally rank 6 regardless of the number of measurements.

To show this fact, let $A_{\widehat{H}} = A_{(H_1, H_2, H_3)}$ be a row vector representing the 9 entries of the row of A for the direction $\hat{H} = [H_1\ H_2\ H_3]^T$. It suffices to find 6 directions $\hat{H}^{(1)},\ldots,\hat{H}^{(6)}$ such that any row $A_{\widehat{H}}$ can be expressed as a linear combination of the rows $A_{\widehat{H}^{(1)}},\ldots,A_{\widehat{H}^{(6)}}$. This requirement is satisfied by the 6 directions (1, 0, 0), (0, 1, 0), (0, 0, 1), $\frac{1}{\sqrt{2}}(1,1,0)$, $\frac{1}{\sqrt{2}}(0,1,1)$, $\frac{1}{\sqrt{2}}(1,0,1)$,. Specifically, any new row $A_{(H_1, H_2, H_3)}$ can be written as the following (please see the Appendix for a derivation):

$$\begin{aligned} &H_1(H_1 - H_2 - H_3)A_{(1,0,0)} + H_2(-H_1 + H_2 - H_3)A_{(0,1,0)} \\ &+ H_3(-H_1 - H_2 + H_3)A_{(0,0,1)} + 2H_1H_2A_{\frac{1}{\sqrt{2}}(1,1,0)} + 2H_2H_3A_{\frac{1}{\sqrt{2}}(0,1,1)} \\ &+ 2H_3H_1A_{\frac{1}{\sqrt{2}}(1,0,1)}. \end{aligned} \tag{7}$$

Therefore, to invert the relationship $\vec{b} = \mathbf{A}\vec{x}$, we instead take the least squares solution with minimum norm, or

$$\vec{x}^* = \underset{\vec{x}}{\operatorname{argmin}} \| \vec{x} \|_2 \ \ s.t. \ \vec{x} \in \underset{\vec{x}}{\operatorname{argmin}} \| \mathbf{A}\vec{x} - \vec{b} \|_2 , \tag{8}$$

which can be solved analytically using the pseudoinverse of **A** (specifically, given the singular value decomposition $\mathbf{USV}^{\mathrm{T}}$ of **A**, the pseudoinverse is given by $\mathbf{VS}^*\mathbf{U}^{\mathrm{T}}$, where **S*** inverts the non-zero singular values). To enforce symmetry after inversion, we decompose $\boldsymbol{\chi}$ into symmetric and antisymmetric parts such that $\boldsymbol{\chi} = \boldsymbol{\chi}_{symm} + \boldsymbol{\chi}_{anti}$, where

$$\chi_{symm} = \frac{\chi + \chi^T}{2}, \ \chi_{anti} = \frac{\chi - \chi^T}{2} . \tag{9}$$

and we keep only the symmetric part. The intuition is that, although the underlying susceptibility tensor is symmetric, noise and artifacts introduced during imaging produce asymmetries. Enforcing symmetry during reconstruction causes propagation of error because the solver is forced to fit a symmetric tensor to asymmetric data. Relaxing the symmetry constraint during inversion allows the method to fit a slightly asymmetric tensor, and the asymmetric part can be removed afterward. We justify this hypothesis empirically both in simulation and in real data of the mouse brain and kidney.

2.3 | Regularized STI

We also compare to the regularized STI method proposed in Ref. 18, which we refer to as rSTI. rSTI penalizes anisotropy at higher frequencies in k-space, resulting in more smoothly varying maps, by adding the regularization term

$$W(\vec{k}) \left(\begin{array}{l} \left\| \chi_{\boldsymbol{k}}(\vec{k})_{11} - \chi_{\boldsymbol{k}}(\vec{k})_{22} \right\|_2 + \left\| \chi_{\boldsymbol{k}}(\vec{k})_{22} - \chi_{\boldsymbol{k}}(\vec{k})_{33} \right\|_2 + \left\| \chi_{\boldsymbol{k}}(\vec{k})_{33} - \chi_{\boldsymbol{k}}(\vec{k})_{11} \right\|_2 \\ + \left\| \chi_{\boldsymbol{k}}(\vec{k})_{12} - \chi_{\boldsymbol{k}}(\vec{k})_{23} \right\|_2 + \left\| \chi_{\boldsymbol{k}}(\vec{k})_{23} - \chi_{\boldsymbol{k}}(\vec{k})_{13} \right\|_2 + \left\| \chi_{\boldsymbol{k}}(\vec{k})_{13} - \chi_{\boldsymbol{k}}(\vec{k})_{12} \right\|_2 \end{array} \right) \tag{10}$$

.

The method encourages the diagonal entries to be equal and the off-diagonal entries to be equal at outer k-space, with a weighting function $W(\vec{k})$ that increases for larger $\vec{k}$. The weighting function is given by

$$W(\vec{k}) = 1 - \frac{1}{1 + e^{\frac{k - \alpha}{\beta}}}, \tag{11}$$

where the width α is set to $\frac{k_{\max}}{r}$ and the transition width β is set to $\frac{k_{\max}}{w}$ for hyperparameters r and w. We search over r = 2, 4, 8 and w = 16, 32, 64 and find that r = 2, w = 16 performs the best (lowest compared mean squared error [MSE] in simulation), which matches the choice of hyperparameters in Ref. 18.

3 | METHODS

3.1 | Data acquisition

In this section, we summarize the data acquisition process; for details, see Ref. 19.

This study used adult C57BL/6 mice (Charles River Labs, Durham, NC) and was approved by the Duke University Institutional Animal Care and Use Committee. The brain specimen was acquired from an 18-month-old female mouse using the active staining procedure of Ref. 25, and MRI scans were performed using a quadrature volume coil with 32-mm internal diameter (m2m Imaging, Cleveland, OH) and a 7.0T, 210-mm horizontal bore Magnex magnet. The kidney specimens were acquired from four 15-week-old male mice and imaged using a solenoid RF resonator (21-mm diameter, 21-mm length) and a 9.4T, 89-mm horizontal bore Magnex magnet. The scan protocols and parameters can be found in Table 1 of Ref. 19.

Each specimen was manually rotated and imaged in 17 orientations, with the orientations later determined via registration. The phase data were preprocessed using phase unwrapping and background phase removal via iHARP-ERELLA in the STI Suite v3.0.[26]

3.2 | STI tractography

Similar to DTI, we can decompose the susceptibility tensor into 3 orthogonal eigenvectors with eigenvalues $\chi_1 \geq \chi_2 \geq \chi_3$, where eigenvector direction allows for fiber tracking.[18] In the brain, STI can track white matter fibers, which point in the direction of the major eigenvector associated with the largest eigenvalue.[17] In the kidney, STI is used to track tubules, which point in the direction of the minor eigenvector associated with the smallest eigenvalue.[11] Following Ref. 18 the susceptibility index (SI) is given by

$$SI = \frac{\chi_1 - \chi_3}{\chi_1 + \chi_2 + \chi_3}, \tag{12}$$

rescaled to be from 0 to 1 by subtracting the minimum value and dividing by the maximum. After rescaling, values are truncated to lie between the 25th and 99th percentile. The SI was used to mask regions for tracking. In the brain, the angle threshold was 45°, and regions with SI between 0.25 and 1 were tracked. In the kidney, the angle threshold was 60°, and regions with SI between 0.2 and 0.9 were tracked. Tracking was done using Diffusion Toolkit v0.6.4 and TrackVis v0.6.1.[27]

3.3 | Simulation

We also performed simulations to evaluate the effect of noise on reconstruction accuracy. Using the symmetric part of the aSTI reconstruction of the mouse brain as the ground truth, we simulated phase maps (TE = 8 ms) in 17 directions with the forward model at 7 Tesla (T). We then added additive white Gaussian noise at various noise levels, where the SD was 1%, 3%, or 5% of the maximum value in the image. Finally, we applied the reconstructions (STI, rSTI, aSTI) to the noisy phase and compared MSE and angular difference. We report the mean and SD of MSE and angular difference across 10 runs.

4 | RESULTS

Figure 1 shows the susceptibility tensor for one slice of the mouse brain for STI, rSTI, and our proposed aSTI. For aSTI, the symmetric component (Equation (9)) is shown; and for rSTI, 2 choices of regularization strength are shown (r = 2 and r = 4, with w = 16) (see Equation (11)). aSTI shows sizeable noise reduction and better contrast. For example, in the diagonal terms, we see better separation between the cortical layers and a more clearly defined corpus callosum. rSTI also shows noise reduction compared to STI, especially with high regularization strength (r = 4) but at the cost of blurring.

Figure 2 shows the fiber tracking results and fiber direction maps reweighted by SI. Typically, successful fiber tracking in STI requires regularization with blurring to improve SNR.[18,19,21] Therefore, unregularized STI leads to incomplete tracks. Moreover, aSTI recovers more complete white matter fibers. In the fiber direction maps, aSTI shows more coherent fiber directions.

Figure 3 shows the susceptibility tensor for the mouse kidney (left: STI, right: aSTI). Compared to the brain, the artifact reduction effect of aSTI is much more apparent. In the off-diagonal terms, we see light and dark spot artifacts in the STI reconstruction but not in the aSTI reconstruction. These artifacts are especially apparent in the renal pelvis, where the susceptibility should be uniform. Furthermore, in the STI reconstruction, the high susceptibility of the blood vessels bleeds into neighboring areas, whereas the aSTI reconstruction shows very sharp separation between the blood vessel and other tissue.

Figure 4 displays the reconstructions of the 3 methods (STI, rSTI, symmetric part of aSTI) for simulated phase of the mouse brain with 5% additive white Gaussian noise. Visually, aSTI is the least noisy, followed by rSTI, then STI.

Finally, we quantitatively compare STI, rSTI, and aSTI by computing MSE and angular difference when reconstructing from the simulated phase of the mouse brain with additive noise, as shown in Table 1. We find that the symmetric part of aSTI outperforms aSTI without the decomposition, which in turn outperforms rSTI, which outperforms STI. These quantitative results verify the improvements seen in Figures 1–4.

In Supporting Information Figure S1, we provide the fiber tracking and fiber direction mapping results for the kidney, and once again we see that the aSTI reconstruction produces better results. We also show the symmetric–antisymmetric decomposition of the aSTI reconstruction and find that the antisymmetric part contains mostly noise and artifacts, a finding that we explore further in the below discussion section.

5 | DISCUSSION

The results provide both qualitative and quantitative evidence that the aSTI reconstruction is more effective than the STI reconstruction. In this section, we further discuss their differences.

Other than the reduced noise and artifacts, one difference is that the off-diagonal terms of aSTI are typically smaller in amplitude than those of STI, raising the question of which reconstruction is more correct. In the simulated brain reconstructions (Figure 4), the answer is clear: the reduction in amplitude is due to the noise reduction effect of aSTI, and aSTI is closer to the ground truth both visually and quantitatively.

Moreover, in the real data the answer is less clear because there are more sources of noise, including, for example, nonlinear phase evolution due to tissue microstructural compartments.[28,29] In the brain (Figure 1), we see that in anatomical regions where we would expect anisotropy (e.g., corpus callosum, hippocampal commissure; see Ref. 18), the reconstructions agree in the off-diagonal terms. Moreover, outside these regions, the STI reconstruction is sometimes non-zero, whereas the aSTI reconstruction is close to zero. In the kidney (Figure 3), the reduced amplitude is much more dramatic, and much of the non-zero values in the off-diagonal terms of STI take the form of dark and light streaks that appear to be artifacts. For these reasons, in combination with the simulation results, we hypothesize that the aSTI reconstruction is more qualitatively correct in the off-diagonal terms.

One hypothesized explanation of noise affecting off-diagonal magnitude is that, in areas of the brain that are isotropic, the off-diagonal terms should be 0. However, noise causes the different directions to have different measured phase, resulting in false anisotropy and therefore larger off-diagonal terms if the algorithm is not robust to noise.

Next, in Supporting Information Figure S2, we depict the symmetric–antisymmetric decomposition of the χ_{12} and χ_{21} terms in the aSTI reconstruction. Before the decomposition, the aSTI reconstruction is already much less noisy than the STI reconstruction. After the decomposition, the antisymmetric part contains mostly noise and streaking artifacts. When this part is discarded, the symmetric part exhibits further reduced noise and streaking artifacts compared to the original χ_{12} and χ_{21} terms. Therefore, we hypothesize that the STI reconstruction is less effective because it must fit a symmetric tensor to data that is asymmetric due to noise and artifacts. Moreover, the aSTI reconstruction is given more flexibility, allowing it to fit a slightly asymmetric tensor. This hypothesis is also supported by the simulation results in Table 1, where the aSTI reconstruction achieves better MSE in the presence of noise. Although magnetic susceptibility is field strength-independent, our data were acquired at 7T and 9.4T, for which SNR is inherently higher.[30] The improvement from aSTI at lower field strengths is expected to be larger.

One limitation of this work is that the fiber-tracking results, although improved, are still incomplete compared to DTI. Therefore, future work is needed to make STI tractography clinically viable. This work also uses a simple minimum norm method to perform the ill-conditioned nonsymmetric inversion because the goal of the study was to focus on the symmetry aspect. Therefore, it would be useful to explore the inverse problem more fully in future work to produce a more sophisticated method. Finally, although aSTI in principle does not require more than 6 measurements because the system of equations has rank 6, the noise performance needs to be further evaluated for smaller numbers of orientations.

6 | CONCLUSION

In this study, we propose relaxing the symmetry constraint during inversion and imposing the constraint post-reconstruction via the symmetric symmetric–antisymmetric tensor decomposition. We support this proposal empirically by showing improved STI reconstructions of the mouse brain and kidney, the first fiber tracking results without blurring, and quantitative improvements in simulated data. Overall, our method is simple, produces improved reconstructions, and sheds light into some shortcomings of current STI methods.

Supplementary Material

Refer to Web version on PubMed Central for supplementary material.

ACKNOWLEDGMENT

Research reported in this publication was in part supported by the National Institutes of Health under Award Number U01EB025162. The content is solely the responsibility of the authors and does not necessarily represent the official views of the National Institutes of Health.

Funding information

National Institutes of Health, Grant/Award Number: U01EB025162

APPENDIX

Let $A_{\widehat{H}} = A_{(H_1, H_2, H_3)}$ be a row vector representing the 9 entries of the row of A for the direction $\hat{H} = [H_1\ H_2\ H_3]^T$. Reshaping the 9 entries as a 3 × 3 matrix for ease of notation, the row can be written as

$$A_{(H_1, H_2, H_3)} = \begin{bmatrix} H_1 \\ H_2 \\ H_3 \end{bmatrix} \left[\frac{H_1}{3} - \frac{k_1}{k^2} \overrightarrow{k}^T \widehat{H} \frac{H_2}{3} - \frac{k_2}{k^2} \overrightarrow{k}^T \widehat{H} \frac{H_3}{3} - \frac{k_3}{k^2} \overrightarrow{k}^T \widehat{H} \right]. \tag{A.1}$$

It suffices to find 6 directions $\hat{H}^{(1)}, \ldots, \hat{H}^{(6)}$ such that any row $A_{\hat{H}}$ can be expressed as a linear combination of the rows $A_{\widehat{H}^{(1)}}, \ldots, A_{\widehat{H}^{(6)}}$. This requirement is satisfied by the 6 directions (1, 0, 0), (0, 1, 0), (0, 0, 1)), $\frac{1}{\sqrt{2}}(1, 1, 0)$, $\frac{1}{\sqrt{2}}(0, 1, 1)$, $\frac{1}{\sqrt{2}}(1, 0, 1)$, whose rows can be written as

$$A_{(1,0,0)} = \begin{bmatrix} \frac{1}{3} - \frac{k_1^2}{k^2} & -\frac{k_1 k_2}{k^2} & -\frac{k_1 k_3}{k^2} \\ 0 & 0 & 0 \\ 0 & 0 & 0 \end{bmatrix}, \tag{A.2}$$

$$A_{(0,1,0)} = \begin{bmatrix} 0 & 0 & 0 \\ -\frac{k_2 k_1}{k^2} & \frac{1}{3} - \frac{k_2^2}{k^2} & -\frac{k_2 k_3}{k^2} \\ 0 & 0 & 0 \end{bmatrix}, \tag{A.3}$$

$$A_{(1,0,0)} = \begin{bmatrix} 0 & 0 & 0 \\ 0 & 0 & 0 \\ -\frac{k_3 k_1}{k^2} & -\frac{k_3 k_2}{k^2} & \frac{1}{3} - \frac{k_3^2}{k^2} \end{bmatrix}, \tag{A.4}$$

$$A_{\frac{1}{\sqrt{2}}(0,1,1)} = \frac{1}{2}\begin{bmatrix} 0 & 0 & 0 \\ -\frac{k_1(k_2+k_3)}{k^2} & \frac{1}{3} - \frac{k_2(k_2+k_3)}{k^2} & \frac{1}{3} - \frac{k_3(k_2+k_3)}{k^2} \\ -\frac{k_1(k_2+k_3)}{k^2} & \frac{1}{3} - \frac{k_2(k_2+k_3)}{k^2} & \frac{1}{3} - \frac{k_3(k_2+k_3)}{k^2} \end{bmatrix}, \tag{A.5}$$

$$A_{\frac{1}{\sqrt{2}}(1,0,1)} = \frac{1}{2}\begin{bmatrix} \frac{1}{3} - \frac{k_1(k_1+k_3)}{k^2} & -\frac{k_2(k_1+k_3)}{k^2} & \frac{1}{3} - \frac{k_3(k_1+k_3)}{k^2} \\ 0 & 0 & 0 \\ \frac{1}{3} - \frac{k_1(k_1+k_3)}{k^2} & -\frac{k_2(k_1+k_3)}{k^2} & \frac{1}{3} - \frac{k_3(k_1+k_3)}{k^2} \end{bmatrix}, \tag{A.6}$$

$$A_{\frac{1}{\sqrt{2}}(1,1,0)} = \frac{1}{2}\begin{bmatrix} \frac{1}{3} - \frac{k_1(k_1+k_2)}{k^2} & \frac{1}{3} - \frac{k_2(k_1+k_2)}{k^2} & -\frac{k_3(k_1+k_2)}{k^2} \\ \frac{1}{3} - \frac{k_1(k_1+k_2)}{k^2} & \frac{1}{3} - \frac{k_2(k_1+k_2)}{k^2} & -\frac{k_3(k_1+k_2)}{k^2} \\ 0 & 0 & 0 \end{bmatrix}. \tag{A.7}$$

With the rows written in this way, we can check via simple algebra that any new row $A_{(H_1, H_2, H_3)}$ can be written as

$$\begin{aligned} &H_1(H_1 - H_2 - H_3)A_{(1,0,0)} + H_2(-H_1 + H_2 - H_3)A_{(0,1,0)} \\ &+ H_3(-H_1 - H_2 + H_3)A_{(0,0,1)} + 2H_1H_2A_{\frac{1}{\sqrt{2}}(1,1,0)} + 2H_2H_3A_{\frac{1}{\sqrt{2}}(0,1,1)} \\ &+ 2H_3H_1A_{\frac{1}{\sqrt{2}}(1,0,1)}. \end{aligned} \tag{A.8}$$

REFERENCES

1. Liu C Susceptibility tensor imaging. Magn Reson Med. 2010;63:1471–1477. [PubMed: 20512849]

2. Langkammer C, Schweser F, Krebs N, et al. Quantitative susceptibility mapping (QSM) as a means to measure brain iron? A post mortem validation study. Neuroimage. 2012;62:1593–1599. [PubMed: 22634862]

3. Wei H, Lin H, Qin LE, et al. Quantitative susceptibility mapping of articular cartilage in patients with osteoarthritis at 3T. JMRI. 2019;49:1665–1675. [PubMed: 30584684]

4. Guan X, Xuan M, Gu Q, et al. Regionally progressive accumulation of iron in Parkinson's disease as measured by quantitative susceptibility mapping. NMR Biomed. 2017;30:e3489.

5. Liu C, Li W, Tong KA, et al. Susceptibility-weighted imaging and quantitative susceptibility mapping in the brain. JMRI. 2015;42:23–41. [PubMed: 25270052]

6. Acosta-Cabronero J, Williams GB, Cardenas-Blanco A, Arnold RJ, Lupson V, Nestor PJ. In vivo quantitative susceptibility mapping (QSM) in Alzheimer's disease. PLoS One. 2013;8:e81093. [PubMed: 24278382]

7. Xie L, Sparks MA, Li W, et al. Quantitative susceptibility mapping of kidney inflammation and fibrosis in type 1 angiotensin receptor-deficient mice. NMR Biomed. 2013;26:1853–1863. [PubMed: 24154952]

8. Langkammer C, Liu T, Khalil M, et al. Quantitative susceptibility mapping in multiple sclerosis. Radiology. 2013;267:551–559. [PubMed: 23315661]

9. Wisnieff C, Ramanan S, Olesik J, Gauthier S, Wang Y, Pitt D. Quantitative susceptibility mapping (QSM) of white matter multiple sclerosis lesions: interpreting positive susceptibility and the presence of iron. Magn Reson Med. 2015;74:564–570. [PubMed: 25137340]

10. Wei H, Dibb R, Decker K, et al. Investigating magnetic susceptibility of human knee joint at 7 Tesla. Magn Reson Med. 2017;78:1933–1943. [PubMed: 28097689]

11. Xie L, Dibb R, Cofer GP, et al. Susceptibility tensor imaging of the kidney and its microstructural underpinnings. Magn Reson Med. 2015;73:1270–1281. [PubMed: 24700637]

12. Lee J, Shmueli K, Fukunaga M, et al. Sensitivity of MRI resonance frequency to the orientation of brain tissue microstructure. Proc Nat Acad Sci. 2010;107:5130–5135. [PubMed: 20202922]

13. Wei H, Decker K, Nguyen H, et al. Imaging diamagnetic susceptibility of collagen in hepatic fibrosis using susceptibility tensor imaging. Magn Reson Med. 2020;83:1322–1330. [PubMed: 31633237]

14. Bilgic B, Xie L, Dibb R, et al. Rapid multi-orientation quantitative susceptibility mapping. Neuroimage. 2016;100:1131–1141.

15. Dibb R, Qi YI, Liu C. Magnetic susceptibility anisotropy of myocardium imaged by cardiovascular magnetic resonance reflects the anisotropy of myocardial filament α-helix polypeptide bonds. J Cardiovasc Magn Reson. 2015;17:1–14. [PubMed: 25589308]

16. Wei H, Gibbs E, Zhao P, et al. Susceptibility tensor imaging and tractography of collagen fibrils in the articular cartilage. Magn Reson Med. 2017;78:1683–1690. [PubMed: 28856712]

17. Li W, Wu B, Avram AV, et al. Magnetic susceptibility anisotropy of human brain in vivo and its molecular underpinnings. Neuroimage. 2012;59:2088–2097. [PubMed: 22036681]

18. Liu C, Li W, Wu B, Jiang Y, Johnson GA. 3D fiber tractography with susceptibility tensor imaging. Neuroimage. 2012;59:1290–1298. [PubMed: 21867759]

19. Dibb R, Liu C. Joint eigenvector estimation from mutually anisotropic tensors improves susceptibility tensor imaging of the brain, kidney, and heart. Magn Reson Med. 2017;77:2331–2346. [PubMed: 27385561]

20. Dibb R, Li W, Cofer G, Liu C. Microstructural origins of gadolinium-enhanced susceptibility contrast and anisotropy. Magn Reson Med. 2014;72:1702–1711. [PubMed: 24443202]

21. Li X, van Zijl PC. Mean magnetic susceptibility regularized susceptibility tensor imaging (MMSR-STI) for estimating orientations of white matter fibers in human brain. Magn Reson Med. 2014;72:610–619. [PubMed: 24974830]

22. Bao L, Xiong C, Wei W, et al. Diffusion-regularized susceptibility tensor imaging (DRSTI) of tissue microstructures in the human brain. Med Image Anal. 2020;67:101827. [PubMed: 33166777]

23. Wisnieff C, Liu T, Spincemaille P, et al. Magnetic susceptibility anisotropy: cylindrical symmetry from macroscopically ordered anisotropic molecules and accuracy of MRI measurements using few orientations. Neuroimage. 2013;70:363–376. [PubMed: 23296181]

24. Li XU, Vikram DS, Lim IAL, et al. Mapping magnetic susceptibility anisotropies of white matter in vivo in the human brain at 7 T. Neuroimage. 2012;62:314–330. [PubMed: 22561358]

25. Johnson GA, Cofer GP, Gewalt SL, Hedlund LW. Morphologic phenotyping with MR microscopy: the visible mouse. Radiology. 2002;222:789–793. [PubMed: 11867802]

26. Li W, Avram AV, Wu B, Xiao X, Liu C. Integrated Laplacian-based phase unwrapping and background phase removal for quantitative susceptibility mapping. NMR Biomed. 2014;27:219–227. [PubMed: 24357120]

27. Wang R, Wedeen Van J. Diffusion Toolkit v0.6.4 and TrackVis v0.6.1 software https://www.Trackvis.org. Accessed May 20, 2019.

28. Cronin MJ, Wang N, Decker KS, et al. Exploring the origins of echo-time-dependent quantitative susceptibility mapping (QSM) measurements in healthy tissue and cerebral microbleeds. Neuroimage. 2017;149:98–113. [PubMed: 28126551]

29. Sood S, Urriola J, Reutens D, et al. Echo time-dependent quantitative susceptibility mapping contains information on tissue properties. Magn Reson Med. 2017;77:1946–1958. [PubMed: 27221590]

30. Hinoda T, Fushimi Y, Okada T, et al. Quantitative susceptibility mapping at 3 T and 1.5 T: evaluation of consistency and reproducibility. Invest Radiol. 2015;50:522–530. [PubMed: 25900085]

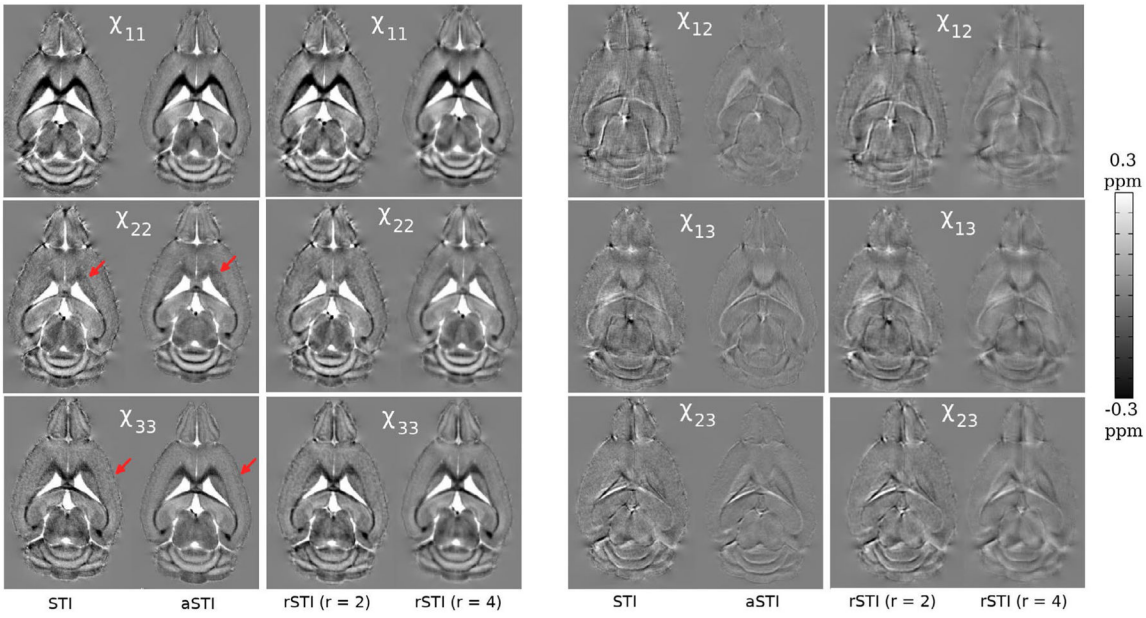

FIGURE 1.

The susceptibility tensor reconstructions of the mouse brain (from left to right: STI, aSTI, rSTI (r = 2), rSTI (r = 4); color scale: −0.3 to 0.3 ppm). The aSTI results show the symmetric component of the reconstructed asymmetric tensor and similarly for other figures. In all 6 terms, the aSTI reconstruction has less noise and better contrast. The red arrow on χ_{22} shows improved delineation of the corpus callosum. The red arrow on χ_{33} shows improved separation between the cortical layers, where the outer layer has a clear stripe of lower susceptibility. For the rSTI results, we show 2 choices of regularization strength. Examining visually, increasing regularization strength increases SNR but at the cost of increased blurring. aSTI, asymmetric susceptibility tensor imaging; rSTI, regularized susceptibility tensor imaging; STI, susceptibility tensor imaging

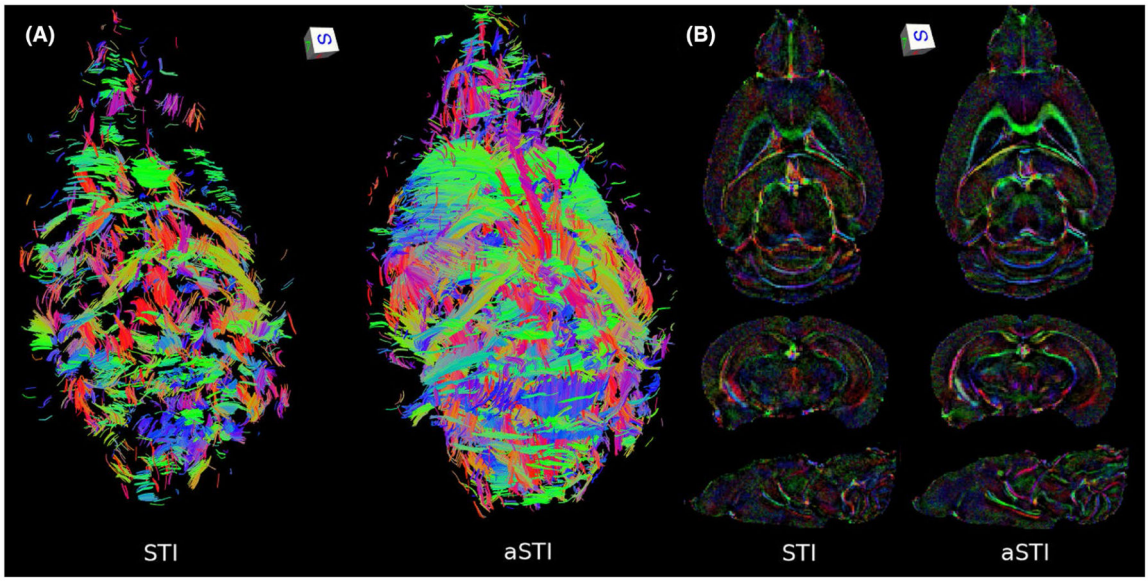

FIGURE 2.

(A) Fiber tracking results of the major eigenvector, where fibers shorter than 5 mm are not shown (left: STI, right: aSTI). The aSTI reconstruction recovers much more of the white matter fiber tracks. (B) The major eigenvector direction of the mouse brain, weighted by SI (left: STI, right: aSTI). The aSTI color maps show more coherent fiber directions, and the SI also serves as a better indicator of white matter. SI, susceptibility index

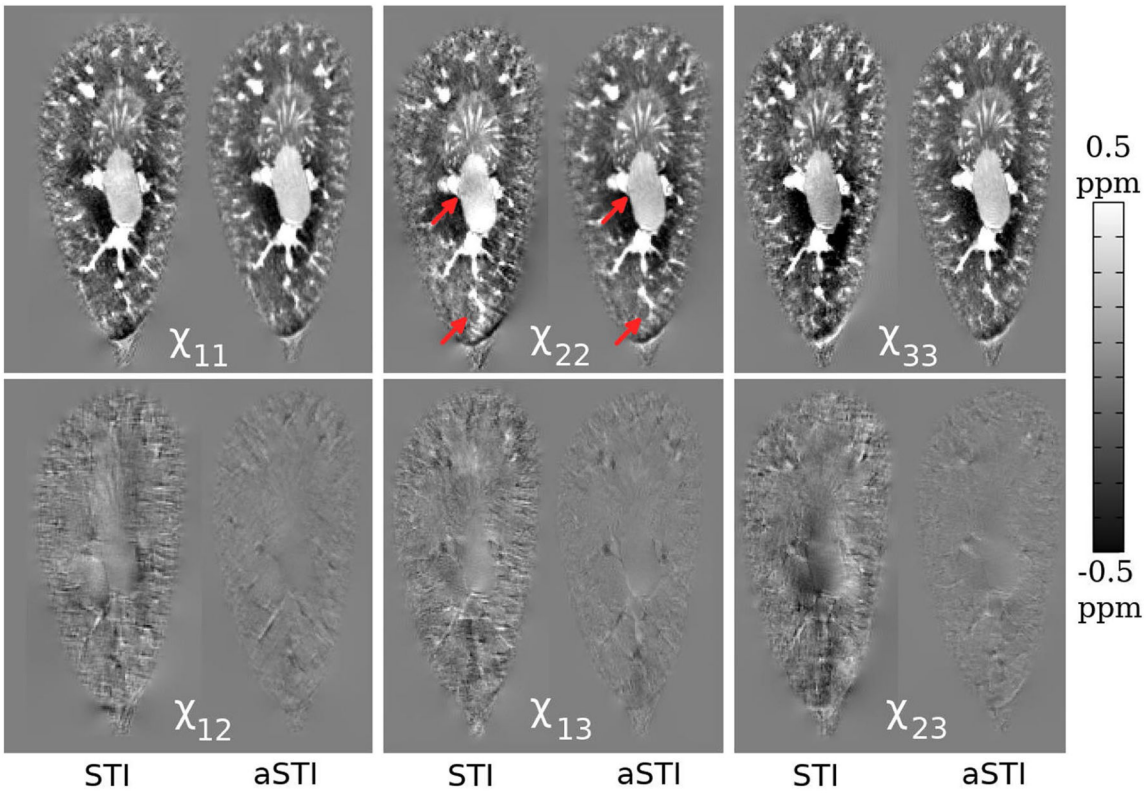

FIGURE 3.

The susceptibility tensor reconstructions of the mouse kidney (left: STI, right: aSTI; color scale: −0.5 to 0.5 ppm). In the off-diagonal terms of the STI reconstruction, we see artifacts in the form of light and dark streaks that are not present in the aSTI reconstruction. The lower red arrows in χ_{22} show that in the STI reconstruction, the high susceptibility of the blood vessels bleeds into neighboring areas. Moreover, the aSTI reconstruction shows very sharp separation between the blood vessel and other tissue. The upper red arrows show an area in the renal pelvis with a dark spot where the susceptibility should be uniform

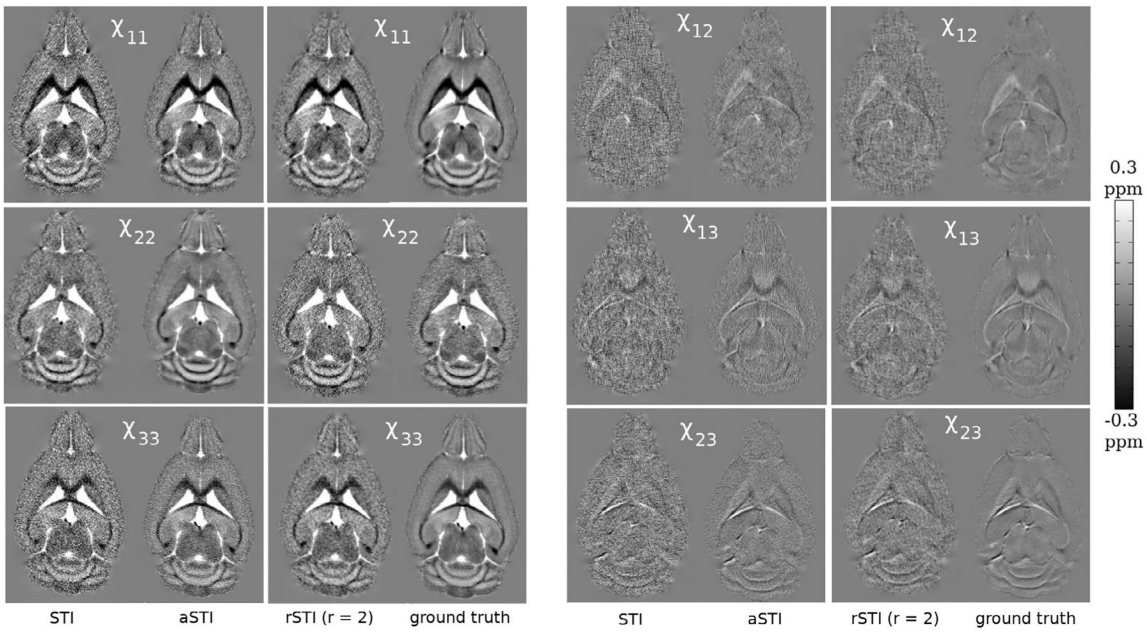

FIGURE 4.

The susceptibility tensor reconstructions of the mouse brain using simulated phase with 5% additive white Gaussian noise (from left to right: STI, aSTI, rSTI, ground truth; color scale: −0.3 to 0.3 ppm). Hyperparameters for the rSTI baseline were chosen via grid search to minimize mean-squared error. Visually, the aSTI reconstruction is the least noisy, followed by rSTI, then STI. These qualitative results are consistent with the quantitative results reported in Table 1

TABLE 1

MSE and angular difference of the STI, rSTI, and aSTI reconstructions of simulated phase of the mouse brain

Noise Level	STI	rSTI	aSTI, no decomp	aSTI, symmetric part
MSE				
1%	$2.62 \times 10^{-5} \pm 8.99 \times 10^{-9}$	$2.04 \times 10^{-5} \pm 1.17 \times 10^{-8}$	$1.07 \times 10^{-5} \pm 2.95 \times 10^{-9}$	$8.38 \times 10^{-6} \pm 3.54 \times 10^{-9}$
3%	$9.14 \times 10^{-5} \pm 7.11 \times 10^{-8}$	$3.89 \times 10^{-5} \pm 3.05 \times 10^{-8}$	$3.27 \times 10^{-5} \pm 2.46 \times 10^{-8}$	$2.60 \times 10^{-5} \pm 2.34 \times 10^{-8}$
5%	$2.22 \times 10^{-4} \pm 2.16 \times 10^{-7}$	$7.59 \times 10^{-5} \pm 7.97 \times 10^{-8}$	$7.66 \times 10^{-5} \pm 3.86 \times 10^{-8}$	$6.14 \times 10^{-5} \pm 3.25 \times 10^{-8}$
Angular Difference (radians)				
1%	0.71 ± 0.0008	0.70 ± 0.0009	0.55 ± 0.0008	0.29 ± 0.0013
3%	0.79 ± 0.0018	0.73 ± 0.0024	0.66 ± 0.0012	0.45 ± 0.0021
5%	0.85 ± 0.0046	0.76 ± 0.0042	0.76 ± 0.0030	0.57 ± 0.0046

To produce the simulated phase, we use the symmetric part of the aSTI reconstruction as the ground truth, and we run the susceptibility tensor map through the forward model. Then, we add additive white Gaussian noise at various noise levels, where the SD is 1%, 3%, or 5% of the maximum value in the image. Finally, we apply the reconstruction methods to the noisy phase and compare their MSE. We report the mean and SD of the MSE and angular difference across 10 runs. To choose the hyperparameters of rSTI, we search over r = 2, 4, 8 and w = 16, 32, 64 and choose the hyperparameters with lowest MSE, resulting in r = 2 and w = 16. Across the 3 noise levels, we find that the symmetric part of the aSTI reconstruction outperforms the aSTI reconstruction, which in turn outperforms rSTI, which outperforms STI. aSTI, asymmetric susceptibility tensor imaging; decomp, decomposition; MSE, mean squared error; rSTI, regularized susceptibility tensor imaging; SI, susceptibility index; STI, susceptibility tensor imaging.